Why do karst catchments exhibit higher sensitivity to climate change? Evidence from a modified Budyko model

Meixian Liu [a,b], Xianli Xu [a,b,*], Alexander Y. Sun [c], Wei Luo [a,b], Kelin Wang [a,b]

[a] *Key Laboratory for Agro-ecological Processes in Subtropical Region, Institute of Subtropical Agriculture, Chinese Academy of Sciences, Changsha 410125, PR China*
[b] *Huanjiang Observation and Research Station for Karst Ecosystem, Chinese Academy of Sciences, Huanjiang 547100, PR China*
[c] *Bureau of Economic Geology, Jackson School of Geosciences, The University of Texas at Austin, Austin, TX, USA*

ABSTRACT

Karst landscape, covers more than 10% of the global land surface and plays an important role in supporting ecosystems and human society, may be strongly influenced by climate change. Vegetation available water (VAW) is a key variable impacting the sensitivity of ecosystems to a changing environment. However, VAW in karst region is difficult to determine and remains uncertain. This study improved a dynamic Budyko-type water balance model, by introducing a nonlinear equation linking climate, vegetation and Budyko-type water balance. This model was calibrated using evolutionary algorithm based on monthly runoff. Comparison results in the Pearl, Yangtze and 12 karst catchments in south China, suggested high effectiveness of this improved model in simulating monthly runoff and evapotranspiration. Furthermore, in the 12 karst catchments, the max VAW was negatively correlated to the portion of karst landscape of the catchment (POK, $r = -0.63$, $\alpha = 0.027$) and the elasticity of evapotranspiration to precipitation ($r = -0.60$, $\alpha = 0.04$). These implied that karst catchments with higher POK had lower VAW, making the ecosystems rely more on precipitation.

1. Introduction

Karst landscape covers more than 10% of the Earth's land surface and has important roles in water supply for human society (about 25% of the world population is dependent on karst water to some extent) (Ford and Williams, 2013; Hartmann et al., 2014). However, owing to the carbonate nature, karst landscape is generally characterized by thin soil, high infiltration capacity and low water holding capacity (Liu et al., 2012; Wilcox et al., 2008; Williams, 2008), and the karst ecosystem often exhibits high vulnerability and sensitivity to changing environment, e.g. climate change, human activities (Fan et al., 2011; Hou et al., 2016; Liu et al., 2014; Liu et al., 2016; Wang et al., 2004). For example, Huang et al. (2013) reported that the NPP (Net Primary Production) in south China generally decreased during 2006–2011, while the magnitude of decrease in NPP in karst region was obviously higher than that in non-karst region. Recently, Liu et al. (2016) pointed out that the actual evapotranspiration in karst catchments in southwestern China was more (less) sensitive to change in precipitation (potential evapotranspiration), and was exposed to higher degradation stress brought by climate change than that in non-karst catchments.

In facts, there are many factors affecting climate sensitivity of ecosystems (Ning et al., 2017; Potter et al., 2005; Yokoo et al., 2008). Besides the physiological properties of vegetation, the vegetation available water (VAW) is a key factor directly affecting ecosystem resilience (Milly, 1994; Potter et al., 2005). Therefore, quantifying VAW is essential in understanding the ecohydrological sensitivity or responses of karst catchments to the changing environment. However, direct estimates of VAW in karst landscape is still a big challenge. To adapt to the environment, vegetation in karst landscape may utilize water from both soil and epikarst zone (water in cracks, conduits), depending on the rooting depth (Nie et al., 2012; Schwinning, 2008). Highly weathered rock may have the ability to store high quantities of water (Querejeta et al., 2006), however, the solution enlarged fissures, cracks and conduits allow rapid transport of water (preferential flow) (Hartmann and Baker, 2017; Heilman et al., 2014), which can also lead to water bypassing the root zone (Arbel et al., 2010; Dasgupta et al., 2006). Due to the high heterogeneity of the karst critical zone (Bakalowicz, 2005), it is hard to quantify the properties of soil (e.g. depth, distribution), epikarst (e.g. porosity, cracks), and vegetation rooted depth, which jointly determine the VAW. Therefore, inverse analysis based on ecohydrological models may be an alternative way (Dorfliger et al., 2009; Pinault et al., 2001).

There are many models for karst ecohydrology modeling, distributed or lumped, on which Hartmann et al. (2014) provided an excellent review. Generally, distributed models need many parameters, which are usually not available in karst region. In comparison, lumped models require only a small number of parameters, and thus are often preferred (Charlier et al., 2012; Hartmann et al., 2013; Jukic and Denic-Jukic, 2009; Tritz et al., 2011). Among these models, the main differences pertain to the treatments of karstic media, evapotranspiration, runoff generation, and groundwater recharge (Hartmann et al., 2014; Hartmann et al., 2012; Scanlon et al., 2003; Zhang et al., 2011). Particularly, evapotranspiration in lumped models is often assumed to be a function of the soil water storage (Hartmann et al., 2013; Janza, 2010) or simply the potential evapotranspiration (Jukic and Denic-Jukic, 2009; Tritz et al., 2011), ignoring the impacts of vegetation dynamics. These treatments would lead to high uncertainties in evapotranspiration modeling. In fact, these models are mainly used to model rainfall-runoff response and karstic aquifer recharge (Jukic and Denic-Jukic, 2009).

To model water balance over variable time scales, Zhang et al. (2008) developed a dynamic Budyko water balance model (Budyko, 1974; Choudhury, 1999; Yang et al., 2008). This model divides the catchment water storage into root zone storage and groundwater storage, and assumes that water partitioning among different hydrological components (e.g. runoff, evapotranspiration) follows the Budyko hypothesis (Zhang et al., 2008). This lumped-parameter, dynamic Budyko model has shown good performance in runoff modeling (Zhang et al., 2008). Most importantly, this model contains several important concepts related to ecohydrological sensitivity. However, this model also ignores the impacts of dynamic vegetation, and its performance in karst region has not been verified. The purposes of this study were two-fold: to improve and validate the dynamic Budyko model in runoff and evapotranspiration modeling in karst catchments, and to investigate how the karst landscape affects ecohydrological parameters. This paper is arranged as follows: Section 2 introduces the data sources, Section 3 focuses on the study area and introduces the model and the improvements as well as the methodologies, Section 4 includes the results, Section 5 provides our discussion, and the conclusion is given in Section 6.

2. Data sources

Monthly precipitation (P), potential evapotranspiration (PET), evapotranspiration (ET), runoff (Q) and change in water storage (ΔS) of 32 global large catchments were collected form Pan's dataset (1984–2006) (Pan et al., 2012). This dataset is based on multiple sources, and has been widely used in previous hydrological studies (Liu et al., 2017; Zeng and Cai, 2016). The Normalized Difference Vegetation Index (*NDVI*) was derived from the GIMMS (Global Inventory Modeling and Mapping Studies) NDVI3g (NDVI, version 3 g) dataset (1982–2012) (Anyamba et al., 2014) to reflect vegetation. Monthly natural runoff (1950s-2000) in 12 karst catchments were collected from the Changjiang River Conservancy Commission and Zhujiang Water Resources Commission. Daily meteorological data (1950s–2000) at 32 meteorological stations in the 12 karst catchments were from the China Meteorological Data Service Network (http://www.escience.gov.cn/metdata/page/index.html). The CERES (Clouds and the Earth's Radiant Energy System) EBAF (Energy Balanced and Filled) Surface Fluxes data set (1°×1° grid, 2000–2014) (http://ceres.larc.nasa.gov/order_data.php) was used to calibrate surface albedo in calculating potential evapotranspiration in the 12 karst catchments. Mean slope was calculated based on the DEM (digital elevation model, 30 m), collected form the Data Sharing Infrastructure of Earth System Science (http://www.geodata.cn/Portal/mdsearch/listMetadata.jsp?category=175&pn=2). Meanwhile, the remote sensing based evapotranspiration (1981–2012) developed by Zhang et al. (2016) (https://data.csiro.au/dap/landingpage?execution=e1s4) was used to evaluate the modeled *ET* in the 12 karst catchments. This remote sensing based *ET* was developed based on the PML algo-

rithm (Leuning et al., 2008) and multisource of inputs (Zhang et al., 2016).

3. Methods

3.1. Descriptions of the original dynamic Budyko model

In the original dynamic Budyko model (Zhang et al., 2008), the precipitation (P) is partitioned into direct runoff (Q_d) and other water components X, which includes the ground water recharge (R), root zone storage change (ΔS) and evapotranspiration (ET):

$$P_{(t)} = Q_{d(t)} + X_{(t)} \tag{1}$$

where the subscripts t means the corresponding component in period t, and $X_{(t)}$ can be considered as catchment water retention. The potential (max) catchment water retention is:

$$X_{0(t)} = S_{mx} - S_{(t-1)} + PET_{(t)} \tag{2}$$

where $PET_{(t)}$ is the potential evapotranspiration; $S_{(t-1)}$ is the residual available water in the preceding period ($t-1$), and S_{mx} is the max vegetation available water (VAW). In karst region, where vegetation can utilize water in soil and bedrock (e.g. cracks) (Nie et al., 2012; Schwinning, 2008), the S_{mx} represents the total max VAW in both soil and the epikarst zone. Assuming that the water partitioning between precipitation ($P_{(t)}$) and catchment water retention ($X_{(t)}$) follows the Budyko hypothesis (Budyko, 1974; Choudhury, 1999), $X_{(t)}$ can be calculated as:

$$X_{(t)} = \frac{P_{(t)} \cdot X_{0(t)}}{\left(P_{(t)}^{\gamma_1} + X_{0(t)}^{\gamma_1}\right)^{1/\gamma_1}} \tag{3}$$

where γ_1 is the catchment water retention efficiency. Therefore, based on water balance, the direct runoff can be calculated as:

$$Q_{d(t)} = P_{(t)} - X_{(t)} \tag{4}$$

In period t, the total available water ($W_{(t)}$) is the sum of the residual water storage $S_{(t-1)}$ and the catchment water retention ($X_{(t)}$):

$$W_{(t)} = X_{(t)} + S_{(t-1)} \tag{5}$$

The total available water $W_{(t)}$ would provide water for evapotranspiration, recharge root zone water storage and groundwater:

$$W_{(t)} = ET_{(t)} + S_{(t)} + R_{(t)} \tag{6}$$

where $ET_{(t)}$ is the evapotranspiration, $S_{(t)}$ is the root zone water storage and $R_{(t)}$ is the groundwater recharge in period t. Defining that the evapotranspiration opportunity $Y_{(t)}$ as (Sankarasubramanian and Vogel, 2002):

$$Y_{(t)} = ET_{(t)} + S_{(t)} \tag{7}$$

Then the potential (max) evapotranspiration opportunity is the sum of potential evapotranspiration and the max vegetation available water:

$$Y_{0(t)} = PET_{(t)} + S_{mx} \tag{8}$$

Likely, assuming that water partitioning between $W_{(t)}$ and $Y_{(t)}$ follows the Budyko hypothesis, $Y_{(t)}$ can be described as:

$$Y_{(t)} = \frac{W_{(t)} \cdot Y_{0(t)}}{\left(W_{(t)}^{\delta_{(t)}} + Y_{0(t)}^{\delta_{(t)}}\right)^{1/\delta_{(t)}}} \tag{9}$$

Within the $Y_{(t)}$, the $ET_{(t)}$ is calculated as:

$$ET_{(t)} = \frac{W_{(t)} \cdot PET_{(t)}}{\left(W_{(t)}^{\delta_{(t)}} + PET_{(t)}^{\delta_{(t)}}\right)^{1/\delta_{(t)}}} \tag{10}$$

where the $\delta_{(t)}$ represents the evapotranspiration efficiency. Then, based on Eqs. (5)–(7), the groundwater recharge ($R_{(t)}$) and root zone water storage change ($\Delta S_{(t)}$) can be calculated as:

$$R_{(t)} = W_{(t)} - ET_{(t)} - S_{(t)} = W_{(t)} - Y_{(t)} \tag{11}$$

Table 1
Definition of the abbreviations.

Abbreviation	Definition	Units
$P_{(t)}$	Precipitation	mm month^{-1}
$\bar{P}$	Long term mean annual precipitation	mm year^{-1}
Q	Runoff	mm month^{-1}
$\bar{Q}$	Long term mean annual runoff	mm year^{-1}
Q_{im}	Modeled runoff by the improved model	mm month^{-1}
Q_{or}	Modeled runoff by the original model	mm month^{-1}
Q_{ob}	Observed runoff	mm month^{-1}
$Q_{d(t)}$	Direct runoff	mm month^{-1}
$Q_{b(t)}$	Base flow	mm month^{-1}
$R_{(t)}$	Ground water recharge	mm month^{-1}
$X_{(t)}$	Catchment water retention	mm month^{-1}
$X_{0(t)}$	Potential catchment water retention	mm month^{-1}
$\Delta S_{(t)}$	Root zone water storage change	mm month^{-1}
$ET_{(t)}$	Evapotranspiration	mm month^{-1}
$\overline{ET}$	Long term mean annual evapotranspiration	mm year^{-1}
ET_{im}	Modeled evapotranspiration by the improved model	mm month^{-1}
ET_{or}	Modeled evapotranspiration by the original model	mm month^{-1}
ET_{rs}	Remote sensing based evapotranspiration	mm month^{-1}
ET_{ob}	Observed evapotranspiration	mm month^{-1}
$PET_{(t)}$	Potential evapotranspiration	mm month^{-1}
$\overline{PET}$	Long term mean annual potential evapotranspiration	mm year^{-1}
$Y_{(t)}$	Evapotranspiration opportunity	mm month^{-1}
$W_{(t)}$	Total available water	mm month^{-1}
$S_{(t-1)}$	Residual available water in the preceding period	mm month^{-1}
$G_{(t)}$	Groundwater storage in period t	mm month^{-1}
G_0	Initial groundwater storage	mm month^{-1}
S_{mx}	Max vegetation available water	mm
$\delta_{(t)}$	Evapotranspiration efficiency	–
γ_1	Catchment water retention efficiency	–
γ_2	Outflow rate of groundwater (recession constant)	–
ω_1	The slope of the regression equation linking $\delta_{(t)}$ and NDVI	–
ω_2	The intercept of the regression equation linking $\delta_{(t)}$ and NDVI	–
ε_p	Elasticity of evapotranspiration to precipitation	mm mm^{-1}
ε_e	Elasticity of evapotranspiration to potential evapotranspiration	mm mm^{-1}
K_c	Crop coefficient	–
ET_0	Reference evapotranspiration	mm month^{-1}
k	Radiation extinction coefficient	–
LAI	Leaf area index	–
$NDVI$	Normalized Difference Vegetation Index	–
β	Root distribution properties	–
φ	Water stress properties	–
POK	Portion of karst landscape distributed in a catchment	–
n	Catchment efficient	–

$$\Delta S_{(t)} = S_{(t)} - S_{(t-1)} = Y_{(t)} - ET_{(t)} - S_{(t-1)} \tag{12}$$

Finally, the groundwater storage ($G_{(t)}$) is treated as a linear reservoir, and the base flow ($Q_{b(t)}$) is modeled as:

$$Q_{b(t)} = \gamma_2 \cdot G_{(t-1)} \tag{13}$$

where γ_2 is a constant representing the outflow rate of groundwater (recession constant). Therefore, the groundwater storage ($G_{(t)}$) in period t is:

$$G_{(t)} = (1 - \gamma_2)G_{(t-1)} + R_{(t)} \tag{14}$$

where $Q_{b(t)}$ is the base flow, $G_{(t)}$ is the groundwater storage. All the abbreviations are summarized in Table 1.

3.2. Improving the model by linking evapotranspiration and vegetation

The original dynamic Budyko model treats the evapotranspiration efficiency ($\delta_{(t)}$) (Eq. (10)) as a constant (Zhang et al., 2008). However, many studies reported that vegetation dynamics (including phenology) and climate seasonality controlled water partitioning (Milly and Shmakin, 2002; Ning et al., 2017; Potter et al., 2005). For example, Eq. (15) is widely used to model plant water uptake (at sub-annual scale) (Feddes et al., 1978; Liu et al., 2013; Somma et al., 1998; Vrugt et al., 2001):

$$ET = \varphi \cdot \beta \cdot \left(1 - e^{-k \cdot LAI}\right) \cdot T_p = \varphi \cdot \beta \cdot \left(1 - e^{-k \cdot LAI}\right) \cdot K_c \cdot ET_0 \tag{15}$$

where K_c is the crop coefficient, ET_0 is the reference evapotranspiration, k is the radiation extinction coefficient, and LAI is the leaf area index. Eq. (15) shows that evapotranspiration is proportional to potential evapotranspiration (Penman, 1948; Yang et al., 2006). Similarly, the Choudhury's equation (Eq. (10)) can be considered as a proportional relationship between $ET_{(t)}$ and $PET_{(t)}$ (Choudhury, 1999):

$$ET_{(t)} = \frac{W_{(t)}}{\left(W_{(t)}^{\delta_{(t)}} + PET_{(t)}^{\delta_{(t)}}\right)^{1/\delta_{(t)}}} \cdot PET_{(t)} \tag{16}$$

The $\varphi \cdot \beta \cdot (1 - e^{-k \cdot LAI}) \cdot K_c$ in Eq. (15) is closely related to vegetation, because the β and LAI represent the roots and canopy properties, K_c has clear seasonal variation with vegetation growth (Allen et al., 1998), and φ reflect the water stress. Therefore, term $W_{(t)}/(W_{(t)}^{\delta_{(t)}} + PET_{(t)}^{\delta_{(t)}})^{1/\delta_{(t)}}$ in Eq. (16) could reflect vegetation conditions, like the term $\varphi \cdot \beta \cdot (1 - e^{-k \cdot LAI}) \cdot K_c$ in Eq. (15).

Based on the GIMMS NDVI3g dataset and the water budget dataset developed by Pan et al. (2012), there is a linear relationship between $W_{(t)}/(W_{(t)}^{\delta_{(t)}} + PET_{(t)}^{\delta_{(t)}})^{1/\delta_{(t)}}$ and NDVI:

$$
\begin{aligned}
&W_{(t)}/\left(W_{(t)}^{\delta_{(t)}} + PET_{(t)}^{\delta_{(t)}}\right)^{1/\delta_{(t)}} \\
&= \left(P_{(t)} - \Delta S_{(t)}\right)/\left(\left(P_{(t)} - \Delta S_{(t)}\right)^{\delta_{(t)}} + PET_{(t)}^{\delta(t)}\right)^{1/\delta_{(t)}} \\
&= \omega_1 \cdot NDVI_{(t)} + \omega_2
\end{aligned}
\tag{17}
$$
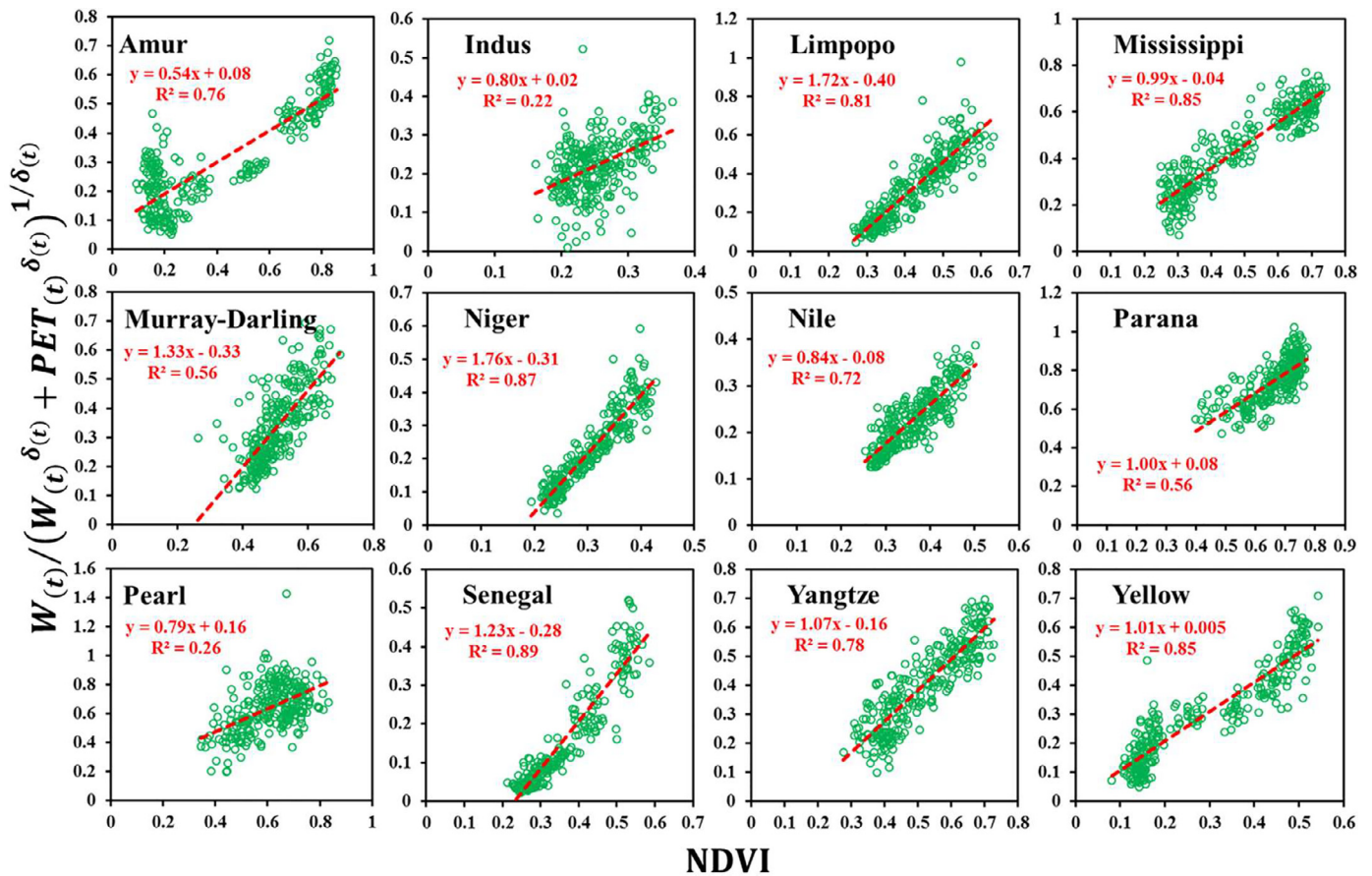
Fig. 1. Relationship between $W_{(t)}/(W_{(t)}^{\delta_{(t)}} + PET_{(t)}^{\delta_{(t)}})^{1/\delta_{(t)}}$ and *NDVI* in 12 global large catchments. Note that the Pan's dataset contains monthly hydrological components in 32 global catchments. However, in some catchments the ET exceeds the PET or even being negative (*ET* < 0) in some months. Finally, a total of 12 basins were selected, with the aridity index (*PET/P*) ranging from 0.68 (Pearl, humid) to 6.35 (Senegal, arid).

where ΔS is the changes in water storage, ω_1 is the slope and ω_2 is an constant. The determination coefficient (R^2) for Eq. (17) being generally higher than 0.7 (8 out of the 12 catchments) (Fig. 1). Thus, Eq. (17) was used to link vegetation ($NDVI_{(t)}$), water supply ($W_{(t)}$), energy ($PET_{(t)}$) and evapotranspiration efficiency ($\delta_{(t)}$) for improving the original model. The main difference between the improved and the original model is that, in the original model the $\delta_{(t)}$ is a constant, while in the improved model, the $\delta_{(t)}$ is the solution of Eq. (17), and depends on vegetation (NDVI), available water ($W_{(t)}$) and energy ($PET_{(t)}$).
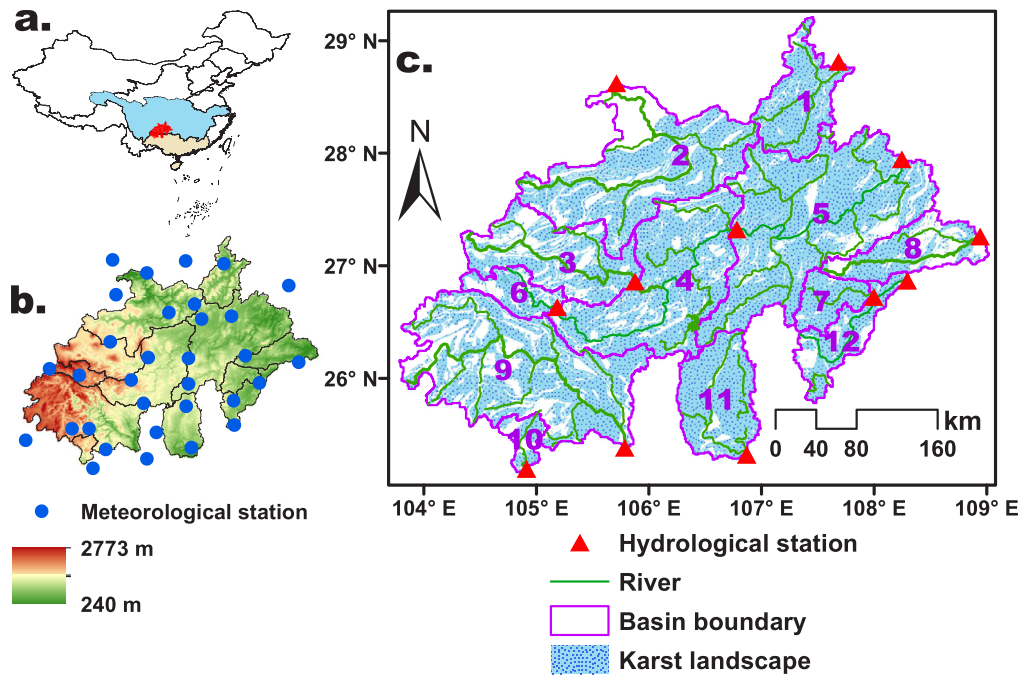
3.3. Study area

The performance of the original and improved models were evaluated in the Pearl, Yangtze, and 12 karst catchments in south China (Fig. 2). The 12 karst catchments, which are belong to the Pearl (No. 9–11) and Yangtze (No. 1–8 and 12) catchments and cover totally about 11.5×10^4 km², are located in Guizhou, Guangxi and Yunnan provinces in southwestern China, where is dominated by karst terrains (Liu et al., 2016; Zhang et al., 2014) and subtropical monsoon climate.

The drainage area of the 12 karst catchments ranges from 0.23×10^4 km² to 2.29×10^4 km² (Table 2). The portion of karst landscape ($POK = Area_{karst}/Area_b$, where $Area_{karst}$ is the karst landscape area and $Area_b$ is the catchment area) ranges from 0.52 to 0.95 (mean of 0.74); the slope ranges from 0.32 to 0.67 (mean of 0.44) (Table 2). The ranges for aridity index (PET/P), annual *NDVI*, runoff coefficient ($Qc = runoff/precipitation$) are 0.74–1.16 (mean of 0.85), 0.47–0.57 (mean of 0.54) and 0.46–0.65 (mean of 0.53), respectively (Table 2). The CV_NDVI (coefficient of variation of the monthly NDVI during 1982–2000) ranges from 0.21 to 0.32 (Table 2).

Note that there were two reasons for calibrating and validating the original and improved models in the Pearl and Yangtze catchments. First, the 12 karst catchments are located in these two big catchments and therefore have the similar climate. Second, the catchment-scale ET series in the two catchments can be collected from the Pan's dataset (Pan et al., 2012). Though uncertainties may still exist, the ET data in Pan's dataset would be close to the trues because they are based on multiple sources of data and assimilation techniques (Pan et al., 2012). Of course, the catchment-scale ET can also be derived from remote sensing technique. However, some uncertainties of the remote sensing based ET were found in this region (see the Fig. 8 in Section 4.2). Therefore, based on the Pan's ET series, we could quantify the performance of the original and improved models in ET modeling with more confidence.

3.4. Data preparation

In the 12 karst catchments, the *PET* were calculated using the Penman method (Penman, 1948), in which the solar radiation were estimated using the Angstrom equation (Allen et al., 1998) and the surface albedo were calibrated using CERES EBAF Surface Fluxes. Details can be found in Liu et al. (2016). Catchment-scale monthly *P, PET* and ET_{rm} (remote sensing based ET) were calculated by arithmetically averaging the monthly data at all stations (grids) in each catchment (the monthly P and PET were aggregated from daily values in the 12 karst catchments). While in the Pearl and Yangtze catchments, the monthly *P, ET* and *PET* were directly collected form Pan's dataset (1984–2006) (Pan et al., 2012). In all the catchments, the monthly *NDVI* were calculated by arithmetically averaging the monthly data at all grids in each catchment. Owing to the different time coverages, the *Q, P, PET, NDVI,*

Fig. 2. Maps of the study area; **a.** location of the Pearl (yellow colored) and Yangtze (blue colored) catchment and the 12 catchments (red colored) in China; **b.** elevation and the distribution of the meteorological stations (blue dots); and **c.** distribution of karst landscape in the 12 catchments, where the purple text is the catchment number showed in Table 1 and the red triangles denote the hydrological stations. (For interpretation of the references to color in this figure legend, the reader is referred to the web version of this article.)

Table 2
Summary of the catchment properties for the 12 karst catchments.

Num.	Station name	Area (km²)	POK (-)	Slope (-)	P (mm/a)	PET (mm/a)	Q (mm/a)	Aridity index (-)	Qc (-)	NDVI (-)	CV_NDVI (-)
1	Changba	5454	0.90	0.67	1386.2	1035.5	700.8	0.85	0.59	0.55	0.31
2	Chishui	16,622	0.63	0.58	1183.1	1029.3	652.3	0.87	0.48	0.55	0.30
3	Hongjiadu	9456	0.64	0.47	1168.6	969.8	598.0	0.90	0.46	0.51	0.29
4	Wujiangdu	15,822	0.79	0.32	1181.0	904.9	587.5	0.77	0.50	0.52	0.28
5	Sinan	22,878	0.84	0.38	1045.1	900.5	605.8	0.86	0.58	0.56	0.27
6	Yangchang	2560	0.66	0.49	1001.8	901.4	464.7	1.16	0.65	0.47	0.30
7	Wanshui	2603	0.95	0.34	1038.1	885.4	617.3	0.78	0.47	0.54	0.32
8	Chongtan	5055	0.52	0.36	1016.9	886.2	493.1	0.81	0.48	0.56	0.28
9	Zhedong	20,372	0.66	0.58	865.2	1001.9	561.3	0.87	0.55	0.52	0.21
10	Maling	2277	0.66	0.41	1269.9	936.8	660.2	0.75	0.51	0.55	0.21
11	Bamao	8682	0.92	0.32	1192.1	925.8	562.6	0.83	0.51	0.57	0.24
12	Shidong	3436	0.75	0.38	1084.1	882.2	525.8	0.74	0.52	0.57	0.25

and ET_{rm} (*ET*) were constrained to the period 1982–2000 for the 12 karst catchments, and 1984–2006 for the Pearl and Yangtze catchments.

3.5. Parameters optimization and their identifiability

There are six parameters need to be calibrated, the S_{mx} (max VAW), γ_1 (water retention efficiency), ω_1 (slope in Eq. (17)), ω_2 (constant in Eq. (17)), γ_2 (recession constant) and G_0 (the initial groundwater storage). Here, these parameters were calibrated based on monthly runoff by using the evolutionary algorithm. The evolutionary algorithms are considered to be robust, globally oriented and generally more straightforward to apply in situations where there is little or no a priori knowledge. Evolutionary algorithms have been widely used in parameter optimization for hydrological models (Cheng et al., 2002; Duan et al., 1992; Tang et al., 2005; Wang, 1991). Here the objective function was designed as:

$$RMSE = \sqrt{\frac{\sum_{i=1}^{N} \left[Q_{m,i} - Q_{ob,i}\right]^2}{N}} \qquad (18)$$

where *RMSE* is the root mean square error, $Q_{m,i}$ is the modeled runoff at time *i*, $Q_{ob,i}$ is the observed runoff at time *i*, *N* is the number of observations.

The calibration was performed by using the GEATbx (Genetic and Evolutionary Algorithm Toolbox for Matlab) (Pohlheim, 2006). The GEATbx contains many variants of genetic algorithms and genetic programming, and can provide many optimization capabilities (Pohlheim, 2006). Details of this MATLAB-based toolbox can be found in Pohlheim (2006). In the calibration, the parameter ranges for the S_{mx}, γ_1, ω_1, ω_2, γ_2 and G_0 were set to be (lower-upper) 0–500 (mm), 0–5 (dimensionless), 0–5 (dimensionless), −0.5 to 1 (dimensionless), 0–1 (mm⁻¹ month⁻¹) and 0–500 (mm), respectively. Meanwhile, the number of individuals per subpopulations (NIND), Maximum number of generations (MAXGEN), Generation gap (GGAP) as well as Precision of binary representation (PRECI) were set to be 35, 100, 0.6 and 10. The calibration procedure was repeated 10,000 times in each catchment, and the parameters that produced the minimum RMSE (Eq. (18)) were used as the final results. Note that in the optimization, the evolutionary algorithms may give some initial assignments such that there is no (nu-

merical and real) solution to Eq. (17). In this case, the objective function (Eq. (18)) was assigned a very large value (e.g. 9999).

Meanwhile, the identifiability of the model parameters was analyzed by using the famous Generalized Likelihood Uncertainty Estimation (GLUE) method (Beven and Binley, 1992; Ortiz et al., 2011; Stedinger et al., 2008; Sun et al., 2016). In the analysis, the RMSE (Eq. (18)) was also used as the likelihood function. A total of 10,000 randomly parameter combinations (within the ranges mentioned above), were produced based on the Latin Hypercube Sampling methods (Li et al., 2010). Similarly, the likelihood function for the parameter combinations that led to no (numerical and real) solution to Eq. (17) were removed in further analysis.

3.6. Evaluation of the improved model

In the Pearl and Yangtze catchments, the time series of *P, PET, ET, Q,* ΔS and *NDVI* were artificially divided into two periods: 1984–1996 for calibration and 1997–2006 for validation. In the 12 karst catchments, the *P, PET, ET_{rm}, Q* and *NDVI* were artificially divided into two periods: 1982–1994 for calibration and 1994–2000 for validation. The six parameters of the improved model and the four parameters of the original model were calibrated using the method mentioned in Section 3.5. The performance the two models were evaluated by comparing the modeled and observed (or remote sensing based) *Q* and *ET* based on correlation analysis and *RMSE* (Eq. (18)). Note that in the Pearl and Yangtze catchments, the *ET* from Pan's dataset (Pan et al., 2012) was used as the observed ET (ET_{ob}); while in the 12 karst catchments, the model performance in ET modeling was evaluated by comparing to the ET_{rm} (remote sensing based ET).

3.7. Linkages between catchment properties and model parameters

The relationships among the optimized model parameters and catchment properties, including portion of karst landscape (*POK*), slope, climate elasticity of evapotranspiration, were investigated based on correlation and (non) linear regression analysis. In particular, the elasticity of evapotranspiration to precipitation (ε_p) and potential evapotranspiration (ε_e) at mean annual scale were calculated based on the Budyko method (Donohue et al., 2011; Liu et al., 2016):

$$\varepsilon_p = \frac{\partial ET}{\partial P} \frac{\bar{P}}{\overline{ET}} = \frac{\overline{PET}^n}{\bar{P}^n + \overline{PET}^n} \tag{19}$$

$$\varepsilon_e = \frac{\partial ET}{\partial PET} \frac{\overline{PET}}{\overline{ET}} = \frac{\bar{P}^n}{\bar{P}^n + \overline{PET}^n} \tag{20}$$

where the $\overline{ET}$, $\overline{PET}$ and $\bar{P}$ are the long-term mean annual *ET, PET* and *P, n* is the catchment efficient derived by numerically solving Eq. (21):

$$\overline{ET} = \bar{P} - \bar{Q} = \frac{\bar{P} \cdot \overline{PET}}{\left(\bar{P}^n + \overline{PET}^n \right)^{1/n}} \tag{21}$$

where $\bar{Q}$ is the long-term mean annual runoff.

4. Results

4.1. Identifiability of the model parameters

Table 3 shows the optimized parameters for the improved and original models. Fig. 3 shows the variation of RMSE with variation of the six parameters (improved model) in the 12 karst catchments. Clearly, though there existing some differences, the RMSE of the dots at the lower edge firstly decreased and then increased with increase in S_{mx}, γ_1, ω_1 and γ_2 (Fig. 3). These indicated that the S_{mx}, γ_1, ω_1 and γ_2 were identifiable parameters in the 12 catchments. As expected, the optimized values (red dots) of these 4 parameters were generally at the bottom of the scatters (Fig. 3).

Relatively, the ω_2 and G_0 were less identifiable, because the scatters distributed nearly uniformly (Fig. 3). However, the optimizing procedure could constrain their ranges. As illustrated in Fig. 4, in the Pearl and Yangtze catchments, the optimized ω_1 and ω_2 were 0.70 and 0.25 (Pearl), and 1.29 and −0.28 (Yangtze), respectively (Table 3). While the statistical ω_1 and ω_2 by using linear regression were 0.79 and 0.16 (Pearl), and 1.07 and −0.16 (Yangtze), respectively (Fig. 1). The differences between the $W_{(t)}/(W_{(t)}^{\delta_{(t)}} + PET_{(t)}^{\delta_{(t)}})^{1/\delta_{(t)}}$ that derived from optimized ω_1 and ω_2 (Table 3) and that derived from statistical ω_1 and ω_2 (Fig. 1) were small (Fig. 4).

4.2. Performance of the improved model

With these parameters, the Q_{im} (*Q* modeled by the improved model) generally coincides with the Q_{ob} (observed *Q*) (Fig. 5). In the Pearl and Yangtze catchments, the regression coefficients and coefficient of determination (R^2) for the linear regression model $Q_{im} = k \times Q_{ob}$ were generally higher than 0.95 in both the calibration and validation (Fig. 5). In all the catchments, the correlations between Q_{im} and Q_{ob} (***r***) ranged 0.74 to 0.98 and 0.71 and 0.98 in the calibration and validation, respectively (Table 4). The RMSE ranged from 6.4 mm month^{-1} to 24.7 mm month^{-1} and from 6.5 mm month^{-1} to 28.2 mm month^{-1}, respectively in the calibration and validation (Table 4). Also, the original model could predict runoff well, with the correlation (RMSE) between Q_{or} (*Q* modeled by the original model) and Q_{ob} being slightly higher (lower) than those for the improved model (Table 4).

Meanwhile, the correlation between ET_{im} (ET modeled by the improved model) and ET_{ob} (observed ET) were 0.82 (calibration) and 0.77 (validation), and 0.98 (calibration) and 0.98 (validation), respectively in the Pearl and Yangtze catchments. Also, the regression coefficients for the linear regression model $ET_{im} = k \times ET_{ob}$ were close to 1.0 in both the calibration and validation (Fig. 6a–d). However, the original model had relatively larger uncertainties in *ET* modeling. Especially in the Yangtze catchment, the original model often underestimated ET in summer and overestimated ET in winter (Fig. 6g–h).

In the 12 karst catchments, the ET_{im} was highly and linearly correlated to the ET_{rs} (remote sensing based *ET*), with the R^2 being generally higher than 0.8 (Fig. 7). Also, the ET_{or} (ET modeled by the original model) were highly related to the ET_{rs}. However, the ranges of ET_{or} were narrower than those of ET_{im}. Similar to the results in Fig. 6g–h, the ET_{or} were generally higher and lower than the ET_{im}, respectively in summer and winter (Fig. 7). This phenomenon also showed some relationships with the CV_NDVI (coefficient of variation of NDVI). The departure between ET_{or} and ET_{im}, seemed to be more obvious in the catchments with larger CV_NDVI (Fig. 7). On the other hand, we also note that the modeled ET by both the models, were generally lower than the ET_{rs} (Fig. 7). Further analysis showed that in these 12 catchments, the ET_{rs} often exceeds *PET* (Fig. 8).

4.3. Relationships among model parameters, climate elasticity and catchment properties

The S_{mx} was negatively correlated to *POK* (portion of karst landscape), with the R^2 being 0.35 ($r = -0.63$, $\alpha = 0.027$) (Fig. 9a). Meanwhile, there existed a power relationship between the water retention efficiency (γ_1) and *slope*, with the R^2 being 0.47 ($r = -0.69$ for γ_1 vs. slope$^{-0.788}$, $\alpha < 0.01$) (Fig. 9a). Other correlations (Table 5) were generally insignificant ($\alpha > 0.05$). However, the correlation for γ_2 vs. *slope* was also relatively high ($r = 0.50$, $\alpha = 0.08$). Furthermore, the correlations between ε_p (elasticity of *ET* to *P*), ε_e (elasticity of *ET* to *PET*) and S_{mx} was −0.60 ($\alpha = 0.04$) and 0.60 ($\alpha = 0.04$), respectively (Fig. 9b).

5. Discussion

The dynamic Budyko model proposed by Zhang et al. (2008) treats the evapotranspiration efficiency $\delta_{(t)}$ as a constant. However, at short
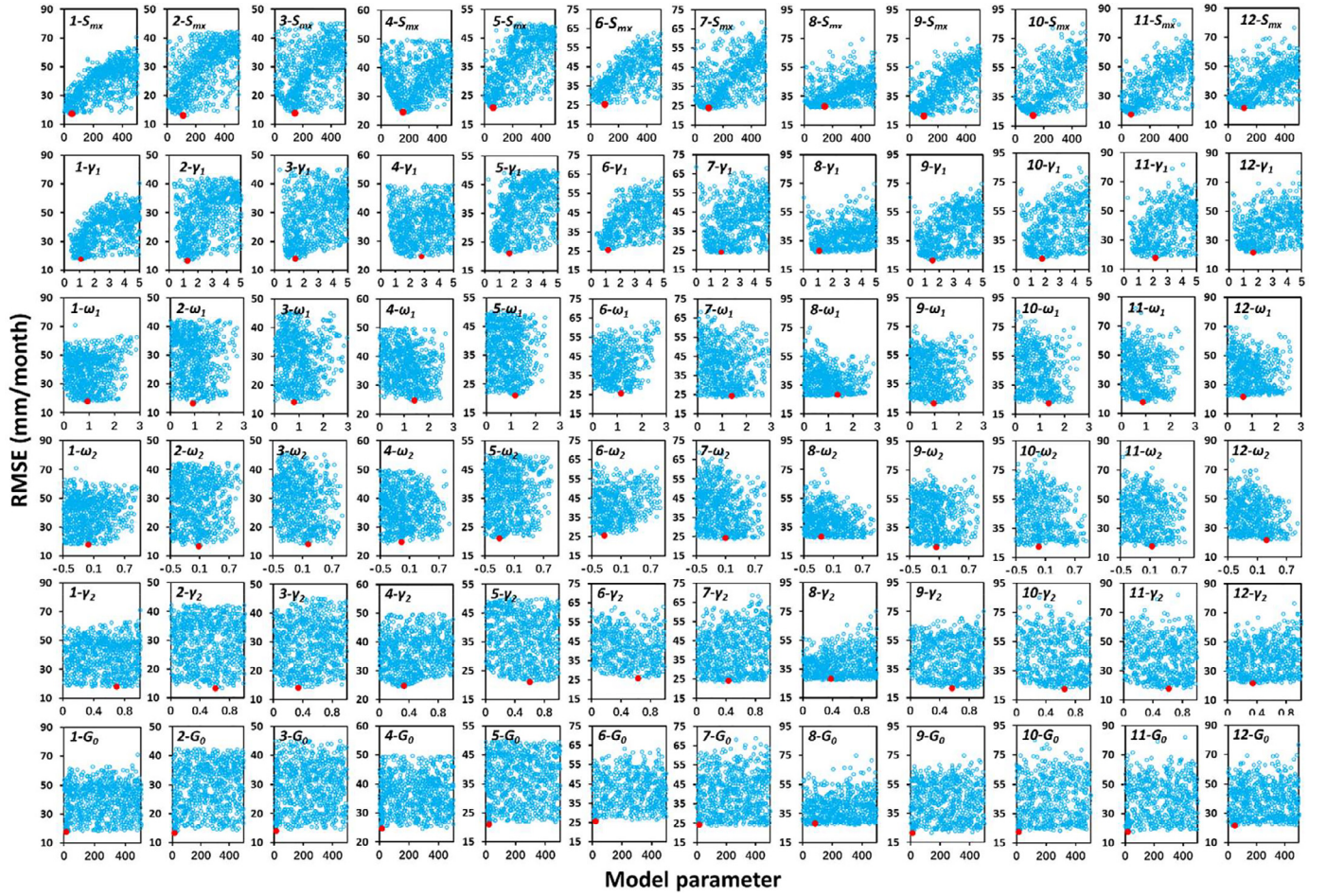
Fig. 3. Scatter plots of the likelihood measure (RMSE) against the six parameters in the 12 karst catchments, the Arabic numbers in the top-left corner of each subfigure is the number of the catchments presented in Table 2; and the red dot in each subfigure is the corresponding optimized parameter shown in Table 3. (For interpretation of the references to color in this figure legend, the reader is referred to the web version of this article.)
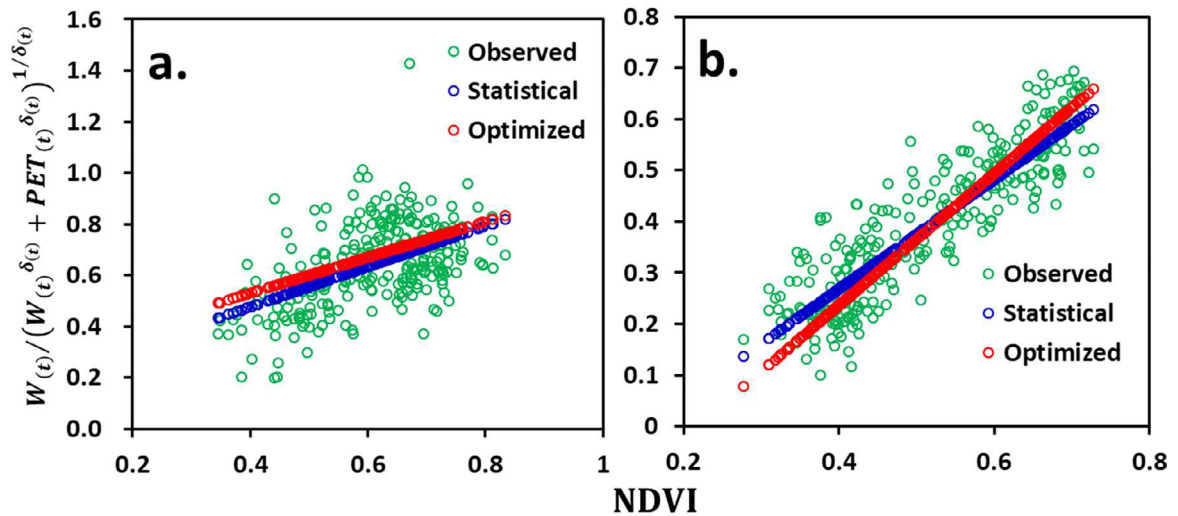

Fig. 4. Scatter plots for *NDVI* against $W_{(t)}/(W_{(t)}{}^{\delta_{(t)}} + PET_{(t)}{}^{\delta_{(t)}})^{1/\delta_{(t)}}$ in the Pearl (**a**) and Yangtze (**b**) catchments, the green dots denotes the observed $W_{(t)}/(W_{(t)}{}^{\delta_{(t)}} + PET_{(t)}{}^{\delta_{(t)}})^{1/\delta_{(t)}}$ showed in Fig. 1, the blue dots (Statistical) denotes the $W_{(t)}/(W_{(t)}{}^{\delta_{(t)}} + PET_{(t)}{}^{\delta_{(t)}})^{1/\delta_{(t)}}$ calculated using the regression model in Fig. 1, and the red dots (Optimized) denotes the $W_{(t)}/(W_{(t)}{}^{\delta_{(t)}} + PET_{(t)}{}^{\delta_{(t)}})^{1/\delta_{(t)}}$ calculated based on the optimized ω_1 and ω_2 in Table 3. (For interpretation of the references to color in this figure legend, the reader is referred to the web version of this article.)

Table 3

The calibrated parameters for the improved and original models in the 12 karst catchments.

No.	Improved model parameters						Original model parameters			
	S_{mx} (mm)	γ_1	ω_1	ω_2	γ_2	G_0 (mm)	S_{mx} (mm)	γ_1	$\delta_{(t)}$	γ_2
Pearl	240.5	0.79	0.70	0.25	0.32	51.5	497.1	0.59	1.43	0.89
Yangtze	309.6	0.63	1.29	−0.28	0.03	184.2	489.9	0.54	0.86	0.03
1	48.4	1.06	0.92	−0.01	0.69	12.3	33.5	1.16	1.40	0.07
2	106.6	1.25	0.91	0.07	0.60	11.4	107.7	1.23	1.43	0.17
3	140.2	1.40	0.79	0.21	0.33	9.9	202.1	1.18	1.36	0.34
4	155.1	2.79	1.43	−0.06	0.34	17.0	163.3	2.62	1.41	0.28
5	59.4	1.67	1.17	−0.20	0.60	21.7	136.5	1.15	1.05	1.00
6	100.9	1.16	1.14	−0.24	0.63	21.8	180.0	1.11	0.75	1.00
7	96.3	1.75	1.40	0.10	0.43	15.0	97.7	2.02	1.61	0.68
8	142.3	1.09	1.38	−0.14	0.38	83.7	108.2	1.95	1.39	0.88
9	100.7	1.53	0.97	0.04	0.57	14.3	143.2	1.56	1.19	1.00
10	124.7	1.78	1.35	−0.04	0.65	15.0	165.2	1.63	1.70	1.00
11	66.2	2.17	0.88	0.14	0.62	19.1	72.3	2.25	1.56	0.80
12	113.7	1.68	0.64	0.29	0.34	47.2	108.7	1.72	1.44	0.39
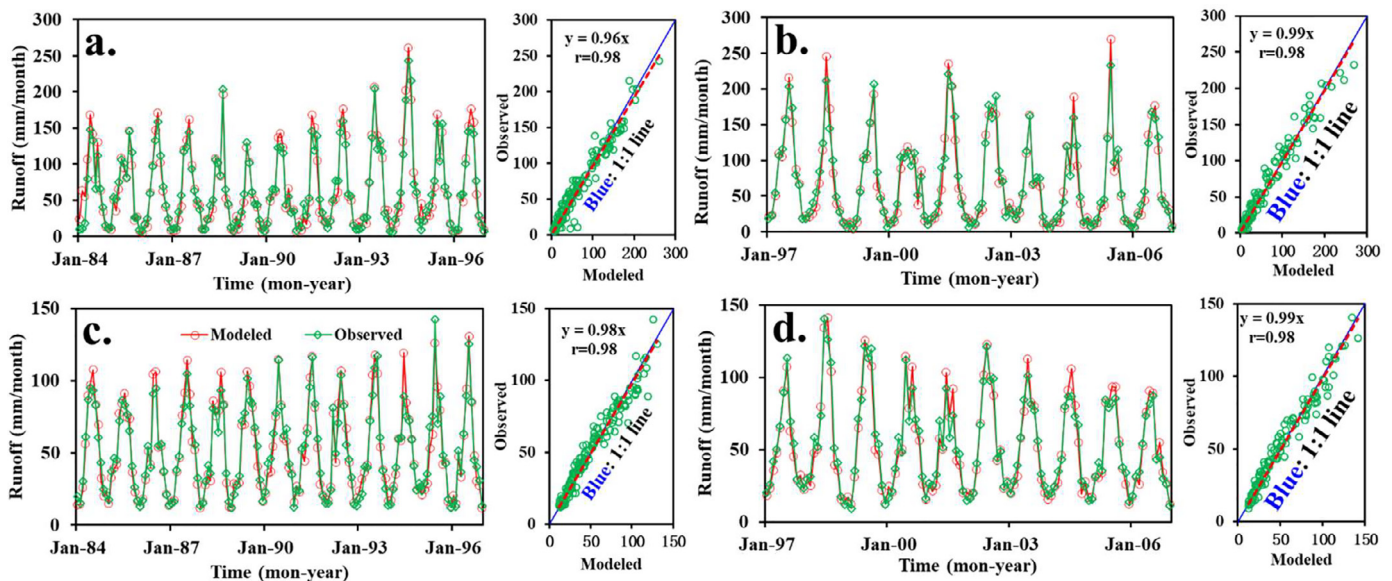
Fig. 5. The observed and modeled runoff by the improved model; **a.** observed and modeled runoff in calibration (1984–1996) in the Pearl catchment; **b.** observed and modeled runoff in validation (1997–2006) in the Pearl catchment; **c–d** are in the same order as **a-b** but for the Yangtze catchment.

Table 4

Performance of the improved and original model in runoff modeling.

Catchment	Improved model				Original model			
	Calibration		Validation		Calibration		Validation	
	$r^{a)}$ (-)	$RMSE^{2)}$ (mm/month)	R (-)	RMSE (mm/month)	R (-)	RMSE (mm/month)	R (-)	RMSE (mm/month)
Pearl	0.98	11.5	0.98	11.9	0.98	10.3	0.98	11.0
Yangtze	0.98	6.4	0.98	6.5	0.98	6.6	0.98	6.2
1	0.90	17.8	0.93	17.9	0.89	18.7	0.92	22.5
2	0.91	12.6	0.93	13.3	0.89	13.4	0.92	17.6
3	0.90	14.0	0.93	14.0	0.90	13.5	0.92	15.6
4	0.81	21.4	0.80	24.7	0.80	21.6	0.78	29.8
5	0.90	17.1	0.88	21.0	0.89	18.6	0.89	27.3
6	0.86	24.7	0.85	25.7	0.87	24.0	0.87	28.7
7	0.85	20.5	0.90	24.3	0.86	20.3	0.90	26.4
8	0.74	24.2	0.71	28.2	0.77	22.2	0.77	30.6
9	0.93	20.2	0.95	21.6	0.94	20.5	0.95	22.8
10	0.93	24.3	0.97	22.5	0.93	24.9	0.97	18.6
11	0.94	17.0	0.95	17.7	0.93	17.8	0.95	19.7
12	0.90	19.6	0.92	21.6	0.90	19.7	0.92	23.1

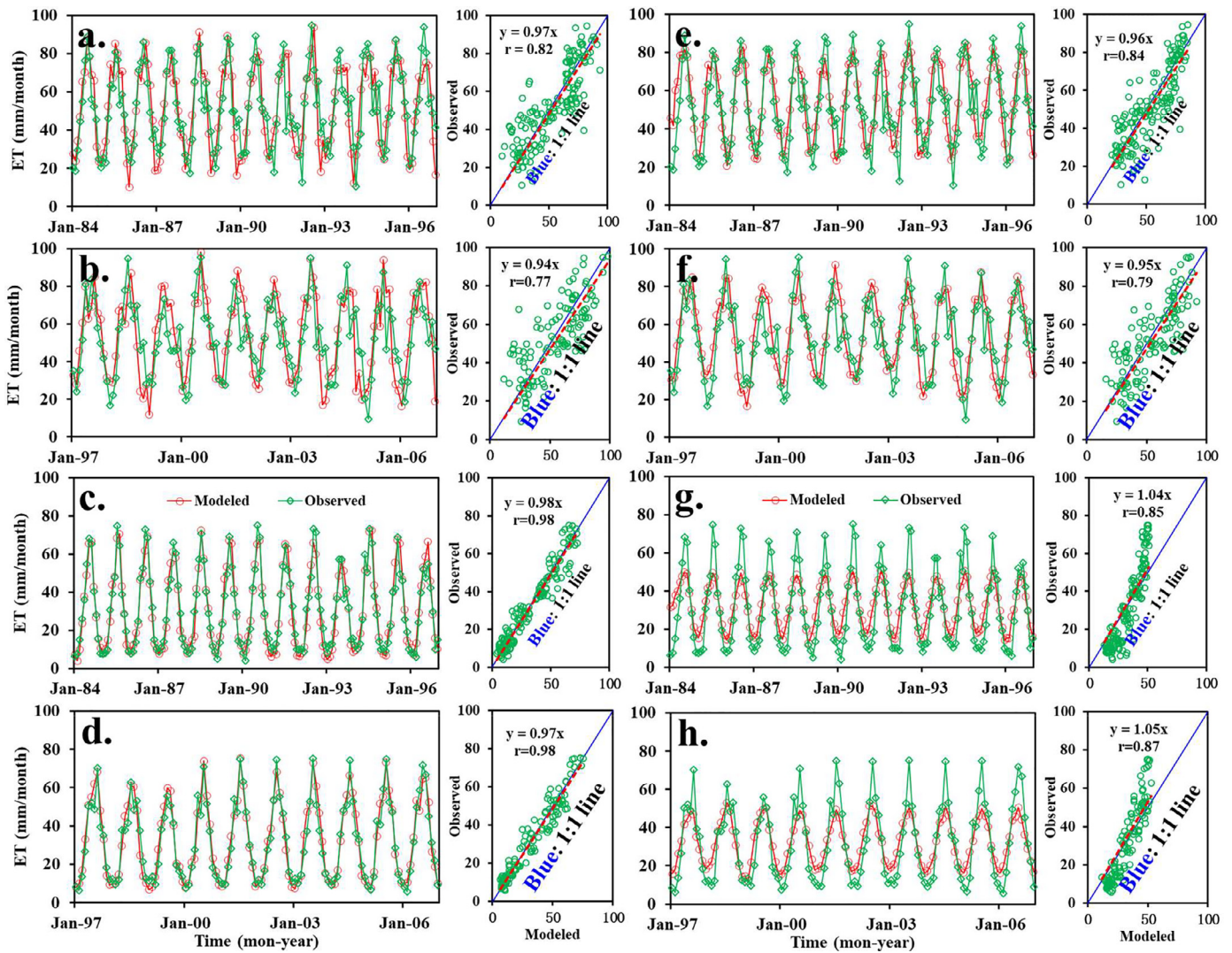[a] *r* is the correlation between the modeled and observed monthly runoff.

Fig. 6. The observed and modeled ET by the improved and original models; **a.** observed and modeled ET in the calibration period (1984–1996); **b.** observed and modeled ET in the validation period (1997–2006); **c–d** are in the same order as **a–b** but for the Yangtze River Basin; the subfigures **e–h** are in the same order as **a–d** but for the original model.

Table 5

Correlations among the model parameters, POK and slope in the 12 karst catchment.

	S_{mx} (mm)	γ_1	ω_1	ω_2	γ_2	G_0 (mm)
POK	−0.63*	0.42	−0.02	0.19	0.18	−0.43
Slope	−0.33	−0.64*	−0.41	−0.02	0.50	−0.37

* Represents that the correlation is significant at $\alpha = 0.05$.

time scales (e.g. monthly), some of the catchment properties are transient, especially the vegetation. The dynamic vegetation (including phenology) should affect water partitioning a lot (Donohue et al., 2007; Ning et al., 2017). This study found a linear relationship (Eq. (17)) at monthly scale (R^2 were generally higher than 0.7) (Fig. 1), reflecting the interactions among energy, water availability and vegetation. This relationship means that under a given *PET*, the higher *NDVI* (better vegetation) is, the higher the *ET*, which is highly related to the vegetation growth and production (Chong et al., 1993; Schimel et al., 1997). However, this relationship (Eq. (17)) was poor at annual or longer time scales (data not shown here), mainly due to that the linearly aggregated (e.g. average and sum) *PET, P* and *NDVI* have missed their seasonality infor-

mation. The high correlation for Eq. (17) evidenced the importance of climate and vegetation seasonality in water-energy balance.

The nonlinear Eq. (17) was employed for improving the original dynamic Budyko model (Zhang et al., 2008). The low RMSE and high correlations between the Q_{ob} (observed Q) and ET_{ob} (observed ET) and the Q_{im} (Q modeled by the improved model) and ET_{im} (ET modeled by the improved model) in the Pearl and Yangtze catchments, demonstrated the effectiveness of the improved model in Q and *ET* modeling (Figs. 5 and 6, Table 4). Similarly, in the 12 karst catchments, the high correlations and relatively low RMSE illustrated that the improved model could capture well Q in karst region (Table 4). As for *ET* modeling, the ET_{im} were highly correlated to, but were always lower than the ET_{rs} (remote sensing based *ET*) (Zhang et al., 2016) (Fig. 7). However, the ET_{im} may have higher accuracy than the ET_{rs}, because the latter often exceeds *PET* in this region (Fig. 8).

Relatively, the RMSE (correlation) between Q_{im} and Q_{ob} were slightly lower (higher) than those between Q_{or} (Q modeled by the original model) and Q_{ob}, indicating that the effectiveness in Q modeling of the improved and original models were similar to each other. However, the larger ranges of ET_{im} and higher correlation between ET_{im} and ET_{rs} indicated the advantages of the improved model in ET modeling (Figs. 6 and 7). The original model neglects vegetation dynamics, and
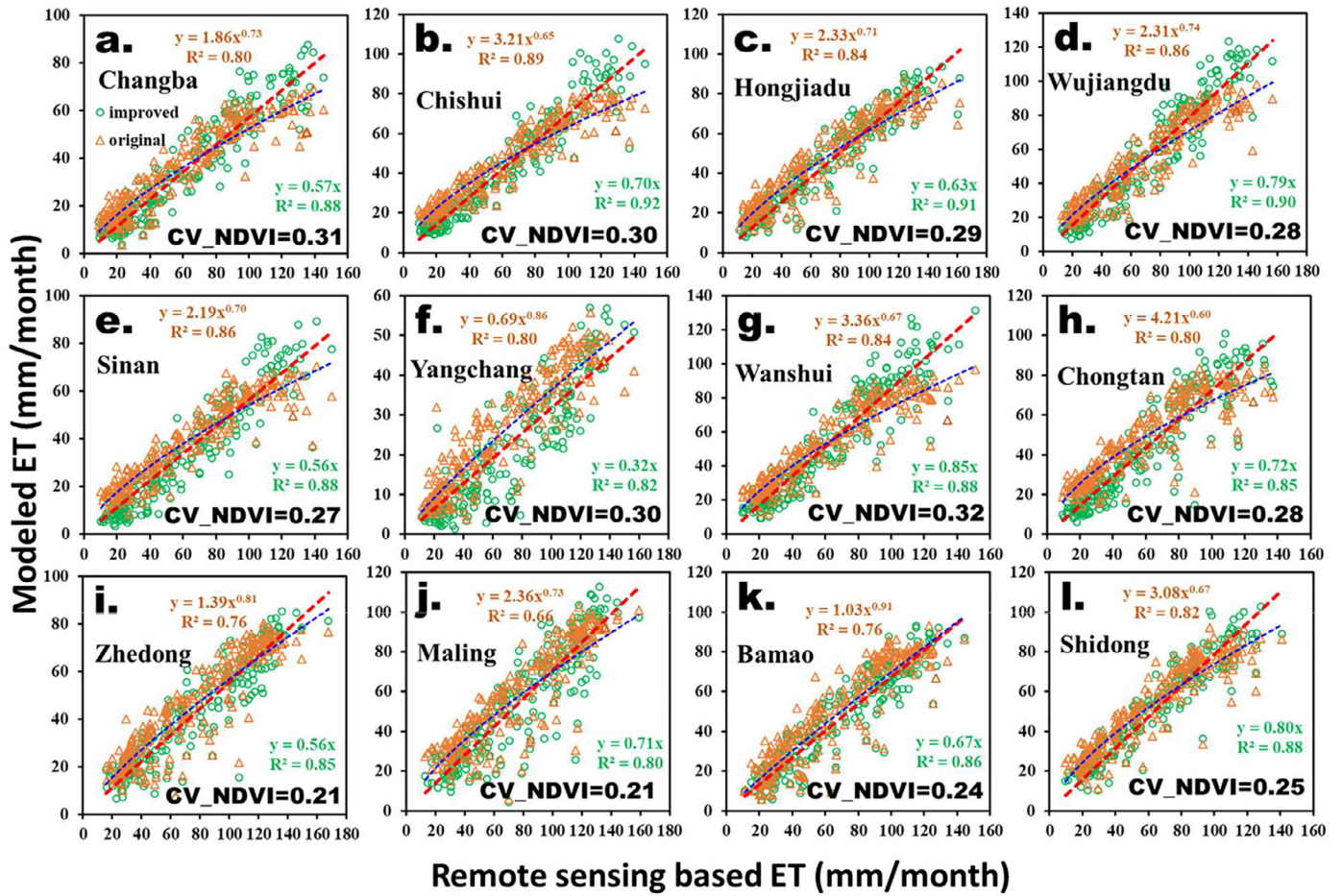
Fig. 7. Scatter plot for the modeled *ET* against the remote sensing based *ET* in the 12 karst catchments, the CV_NDVI is the coefficient of variation of NDVI (Table 2) in each catchment.
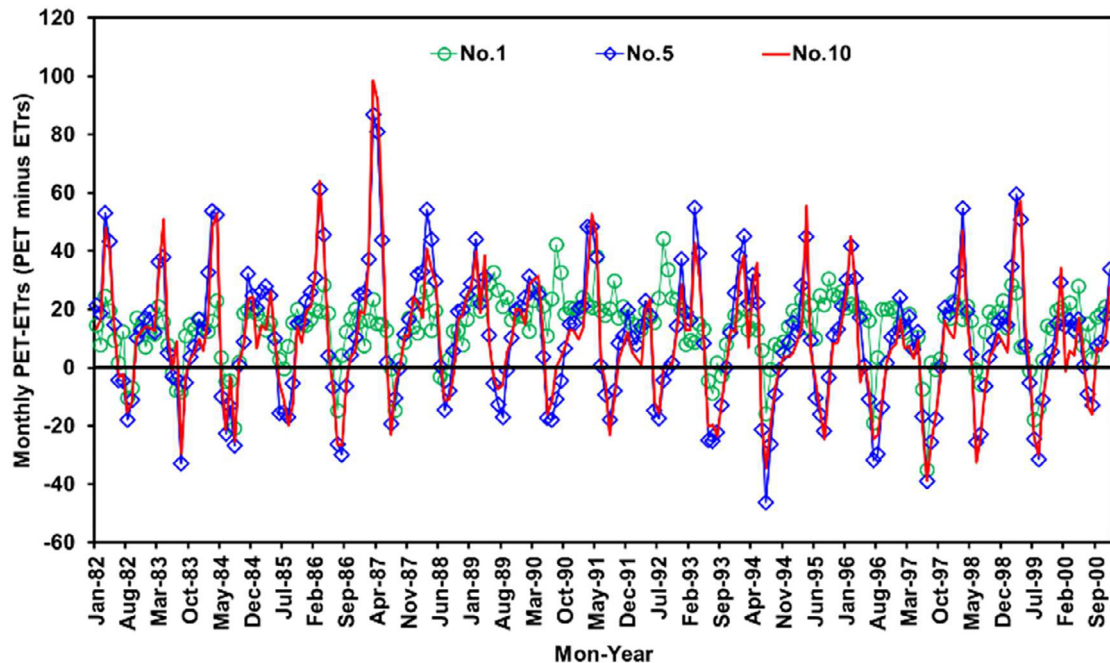

Fig. 8. The differences between *PET* and ET_{rs} ($PET - ET_{rs}$) in the Changba (No. 1), Sinan (No. 5) and Maling (No. 10) catchment.
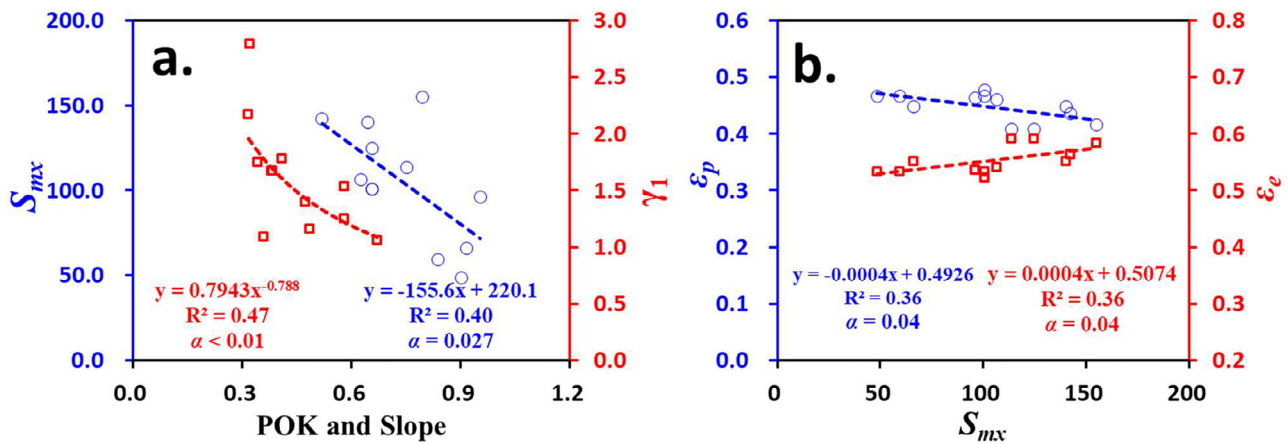
Fig. 9. Relationships among S_{mx}, γ_1, ε_p, ε_e, POK and mean slope in the 12 catchments.

treats the evapotranspiration efficiency ($\delta_{(t)}$) (Eq. (10)) as a constant. Results demonstrated that this treatment brought out underestimation of ET in summer and overestimation of ET winter (Figs. 6 and 7), especially in catchments with larger vegetation variability (e.g. CV_NDVI, the coefficient of variation of NDVI) (Fig. 7).

Most importantly, each of the parameters in the improved model has a physical interpretation. The γ_1 is the catchment water retention efficiency, a larger (smaller) γ_1 represents more (less) precipitation retention and less (more) direct runoff under a given precipitation. In the 12 karst catchments, the γ_1 was highly (and negatively) related to *slope* ($r = -0.69$ for γ_1 vs. slope$^{-0.788}$, $\alpha < 0.01$) (Fig. 9). This is reasonable because high slope means well drained (Yokoo et al., 2008) and therefore less residual precipitation in the catchment (Xu et al., 2013; Zhang et al., 2008). The ω_1 reflects the ecohydrological interactions between vegetation and climate; larger ω_1 indicates higher sensitivity of *ET* to vegetation. There is no clear relationship among ω_1, *POK* and *slope* (Table 5), and the vegetation types (data not shown here). However, we deduce that the vegetation types, distribution, physio-ecological properties, and the vegetation-terrain coupling characteristics might be the control factors for ω_1. The recession constant γ_2 (Nathan and Mcmahon, 1990; Zhang et al., 2008), representing the outflow rate of groundwater, was positively correlated to *POK* ($r = 0.18$, $\alpha > 0.05$) and *slope* ($r = 0.50$, $\alpha = 0.08$) (Table 5), indicating that larger amount of groundwater could discharge as base flow in catchment with higher *POK* and steeper terrain. This is consistent with other findings (Price, 2011). For example, Tetzlaff et al. (2009) found that in steeper montane regions, the transit times tend to be lower. Previous studies also reported that the influence of topography on base flow is most pronounced in relatively high relief settings, such as the karst or highly porous settings (Devito et al., 2005; Price, 2011; Tetzlaff et al., 2009).

Furthermore, the S_{mx} represents the max available water storage in the vegetation root zone (soil and epikarst zone in karst region). When there is no precipitation in a period, for example, in a drought, the S_{mx} means the max available water for the vegetation. Generally speaking, the vegetation in land with high available water, may have better ability to adapt to climate change (variability, seasonality) (Yokoo et al., 2008). The negative correlation between S_{mx} and *POK* ($r = -0.63$, $\alpha < 0.05$) (Fig. 9a) indicated that ecosystem in karst catchments (have relatively lower S_{mx}) might rely more on precipitation than in non-karst catchments. This is demonstrated by the negative correlation between ε_p (elasticity of evapotranspiration to precipitation) and S_{mx} ($r = -0.60$, $\alpha = 0.04$) (Fig. 9b), which suggested that a same change (increase/decrease) in P would bring about greater change (increase/decrease) in *ET* in karst region. Similarly, Liu et al. (2016) also pointed out that karst catchments might exhibit higher degradation stress from climate change than the non-karst catchments in southwestern China.

In fact, the S_{mx} is a vegetation related parameter (Zhang et al., 2008) and is an overall property controlled by the spatial heterogeneous vegetation-terrain coupling in a catchment. Vegetation types, rooting depth, properties of soil and epikarst zone, could affect S_{mx} to some extent. For example, deep rooted plant (e.g. some native trees) may have higher S_{mx}, while shallow rooted plants (e.g. grass) may have lower S_{mx}. Therefore, the S_{mx} may exhibit strong spatial heterogeneity. The relative low correlation (-0.63) suggests that *POK* is just one of the factors affecting S_{mx}. Furthermore, we also note that the *POK* is far from efficient to represent the highly heterogeneous karstic media. The porosity, position and hydrological connectivity of the fractures, conduits and caves, soil depth and the hydraulic properties, as well as vegetation conditions, are key factors affecting the hydrological processes in karst aquifers. Therefore, even the *POK* in two catchments were the same to each other, the parameters of the two catchments would be quite different. For example, in the catchments No. 9 and No.10 with the *POK* being the same 0.66, the S_{mx}, γ_1, ω_1 and γ_2 in No.10 were obviously larger than those in No.9 (Table 3).

Beside these, uncertainties of the optimized parameters would also affect the reliability of these results. Results demonstrated that, the S_{mx}, γ_1, ω_1 and γ_2 were generally identifiable in the 12 karst catchments (Fig. 3). However, the sensitivity of runoff to these parameters in different catchments differed from each other (Fig. 3), and even, the runoff exhibited insensitivity to some parameters. For example, the parameters ω_2 was relatively non-identifiable. In this case, though the optimizing procedure could constrain their ranges, there also existing some differences between the true and the optimized (Fig. 4). These slight differences would affect the optimized results of other parameters. Nevertheless, the paper proposed an improved model with high effectiveness in runoff and evapotranspiration modeling in karst catchments, and provided evidences for why the ecosystem in karst catchment is overall fragile and sensitive to climate change.

6. Summary and conclusion

This study improved a dynamic Budyko model by linking available water, potential evapotranspiration, and vegetation (NDVI) at monthly scale. The six parameters, including max available water storage S_{mx}, evapotranspiration efficiency (ω_1 and ω_2), catchment water retention efficiency γ_1, recession constant γ_2 and the initial groundwater storage (G_0), were calibrated based on monthly runoff by using evolutionary algorithm. The performance of the model was evaluated in 14 catchments (Pearl, Yangtze and 12 karst catchments), and the relationships among model parameters and the catchment properties, including the portion of karst landscape (*POK*), slope and the climate elasticity of evapotranspiration, were analyzed in 12 karst catchments. The high correlations (generally higher than 0.85) and low RMSE (root mean square error)

between observations and simulations in the 14 catchments proved the effectiveness of the improved model in runoff and evapotranspiration modeling. Relatively, the original model could simulate runoff as well as the improved model, but exhibited larger uncertainties in ET modeling. Moreover, the max available water storage S_{mx} was negatively correlated to POK ($r = -0.63$, $\alpha < 0.05$) and the ε_p (elasticity of evapotranspiration to precipitation) ($r = -0.60$, $\alpha = 0.04$); and the slope was negatively correlated to the water retention efficiency γ_1 ($r = -0.69$, $\alpha < 0.01$), and positively correlated to the recession constant γ_2 ($r = 0.50$, $\alpha < 0.08$). These results indicated that the catchments with higher POK in southwestern China, have lower vegetation available water and ecosystem relied more on precipitation.

Acknowledgments

References

Allen, R.G., Pereira, L.S., Raes, D., Smith, M., 1998. Crop evapotranspiration: guidelines for computing crop water requirements Food and Agriculture Organization of the United Nations. Rome.

Anyamba, A., Small, J.L., Tucker, C.J., Pak, E.W., 2014. Thirty-two years of Sahelian zone growing season non-stationary NDVI3g patterns and trends. Remote Sens. Basel 6 (4), 3101–3122. https://doi.org/10.3390/rs6043101.

Arbel, Y., Greenbaum, N., Lange, J., Inbar, M., 2010. Infiltration processes and flow rates in developed karst vadose zone using tracers in cave drips. Earth Surf. Processes Landforms 35 (14), 1682–1693.

Bakalowicz, M., 2005. Karst groundwater: a challenge for new resources. Hydrogeol. J. 13 (1), 148–160.

Beven, K., Binley, A., 1992. The future of distributed models - model calibration and uncertainty prediction. Hydrol. Processes 6 (3), 279–298.

Budyko, M.I., 1974. Climate and Life., English ed. Academic, San Diego, Calif.

Charlier, J.B., Bertrand, C., Mudry, J., 2012. Conceptual hydrogeological model of flow and transport of dissolved organic carbon in a small Jura karst system. J. Hydrol. 460, 52–64.

Cheng, C.T., Ou, C.P., Chau, K.W., 2002. Combining a fuzzy optimal model with a genetic algorithm to solve multiobjective rainfall-runoff model calibration. J. Hydrol. 268 (1–4), 72–86.

Chong, D.L.S., Mougin, E., Gastelluetchegorry, J.P., 1993. Relating the global vegetation index to net primary productivity and actual evapotranspiration over Africa. Int. J. Remote Sens. 14 (8), 1517–1546.

Choudhury, B.J., 1999. Evaluation of an empirical equation for annual evaporation using field observations and results from a biophysical model. J. Hydrol. 216 (1–2), 99–110.

Dasgupta, S., Mohanty, B.P., Kohne, J.M., 2006. Impacts of juniper vegetation and karst geology on subsurface flow processes in the Edwards Plateau, Texas. Vadose Zone J. 5 (4), 1076–1085.

Devito, K., et al., 2005. A framework for broad-scale classification of hydrologic response units on the Boreal Plain: is topography the last thing to consider? Hydrol. Processes 19 (8), 1705–1714.

Donohue, R.J., Roderick, M.L., McVicar, T.R., 2007. On the importance of including vegetation dynamics in Budyko's hydrological model. Hydrol. Earth Syst. Sci. 11 (2), 983–995.

Donohue, R.J., Roderick, M.L., McVicar, T.R., 2011. Assessing the differences in sensitivities of runoff to changes in climatic conditions across a large basin. J. Hydrol. 406 (3–4), 234–244.

Dorfliger, N., Fleury, P., Ladouche, B., 2009. Inverse modeling approach to allogenic karst system characterization. Ground Water 47 (3), 414–426.

Duan, Q., Gupta, V.K., Sorooshian, S., 1992. Effective and efficient global optimization for conceptual rainfall-runoff models. Water Resour. Res. 28 (1015–1031).

Fan, F.D., et al., 2011. Assessment and spatial distribution of water and soil loss in karst regions, southwest China. Acta Ecol. Sin. 51, 6353–6362.

Feddes, R.A., Kowalik, P.J., Zaradny, H., 1978. Simulation of Field Water Use and Crop Yield. Simulation Monograph, Pudoc, Wageningen, The Netherlands.

Ford, D., Williams, P.D., 2013. Karst Hydrogeology and Geomorphology. Wiley, New York.

Hartmann, A., Baker, A., 2017. Modelling karst vadose zone hydrology and its relevance for paleoclimate reconstruction. Earth Sci. Rev. 172, 178–192.

Hartmann, A., Barberá, J.A., Lange, J., Andreo, B., Weiler, M., 2013. Progress in the hydrologic simulation of time variant recharge areas of karst systems – Exemplified at a karst spring in Southern Spain. Adv. Water Resour. 54, 149–160.

Hartmann, A., Goldscheider, N., Wagener, T., Lange, J., Weiler, M., 2014. Karst water resources in a changing world: review of hydrological modeling approaches. Rev. Geophys. 52 (3), 218–242. https://doi.org/10.1002/2013rg000443.

Hartmann, A., Lange, J., Weiler, M., Arbel, Y., Greenbaum, N., 2012. A new approach to model the spatial and temporal variability of recharge to karst aquifers. Hydrol. Earth Syst. Sci 16 (7), 2219–2231.

Heilman, J.L., et al., 2014. In: Water-storage Capacity Controls Energy Partitioning and Water Use in Karst Ecosystems on the Edwards Plateau, 7. Ecohydrology, Texas, pp. 127–138.

Hou, W.J., Gao, J.B., Peng, T., Wu, S.H., Dai, E.F., 2016. Review of ecosystem vulnerability studies in the karst region of Southwest China based on a structure-function-habitat framework. Prog. Geography 35 (3), 320–330.

Huang, X.Y., Lin, D.G., Wang, J.A., Chang, S., 2013. Temporal and spatial NPP variation in the karst region in south China under the background of climate change. Scientia Silvae Sinicae 49 (5), 10–16.

Janza, M., 2010. Hydrological modeling in the karst area, Rižana spring catchment, Slovenia. Environ. Earth Sci. 61 (5), 909–920.

Jukic, D., Denic-Jukic, V., 2009. Groundwater balance estimation in karst by using a conceptual rainfall-runoff model. J. Hydrol. 373 (3-4), 302–315.

Leuning, R., Zhang, Y.Q., Rajaud, A., Cleugh, H., Tu, K., 2008. A simple surface conductance model to estimate regional evaporation using MODIS leaf area index and the Penman-Monteith equation. Water Resour. Res. 44 (10).

Li, L., Xia, J., Xu, C.Y., Singh, V.P., 2010. Evaluation of the subjective factors of the GLUE method and comparison with the formal Bayesian method in uncertainty assessment of hydrological models. J. Hydrol. 390 (3-4), 210–221.

Liu, C.C., Liu, Y.G., Fan, D.Y., Guo, K., 2012. Plant drought tolerance assessment for revegetation in heterogeneous karst landscapes of southwestern China. Flora 207 (1), 30–38. https://doi.org/10.1016/j.flora.2011.06.002.

Liu, M., et al., 2017. A new drought index that considers the joint effects of climate and land surface change. Water Resour. Res.

Liu, M.X., et al., 2014. Is southwestern China experiencing more frequent precipitation extremes? Environ. Res. Lett. 9 (6).

Liu, M.X., Xu, X.L., Wang, D.B., Sun, A.Y., Wang, K.L., 2016. Karst catchments exhibited higher degradation stress from climate change than the non-karst catchments in southwest China: an ecohydrological perspective. J. Hydrol. 535, 173–180.

Liu, M.X., Yang, J.S., Li, X.M., Yu, M., Wang, J., 2013. Numerical simulation of soil water dynamics in a drip irrigated cotton field under plastic mulch. Pedosphere 23 (5), 620–635.

Milly, P.C.D., Shmakin, A.B., 2002. Global modeling of land water and energy balances. Part I: the land dynamics (LaD) model. J Hydrometeorol 3 (3), 283–299.

Milly, P.C.D., 1994. Climate, soil-water storage, and the average annual water-balance. Water Resour. Res. 30 (7), 2143–2156.

Nathan, R.J., Mcmahon, T.A., 1990. Evaluation of automated techniques for base-flow and recession analyses. Water Resour. Res. 26 (7), 1465–1473.

Nie, Y.P., Chen, H.S., Wang, K.L., Yang, J., 2012. Water source utilization by woody plants growing on dolomite outcrops and nearby soils during dry seasons in karst region of Southwest China. J. Hydrol. 420, 264–274.

Ning, T.T., Li, Z., Liu, W.Z., 2017. Vegetation dynamics and climate seasonality jointly control the interannual catchment water balance in the Loess Plateau under the Budyko framework. Hydrol. Earth Syst. Sci. 21 (3), 1515–1526.

Ortiz, C., Karltun, E., Stendahl, J., Gardenas, A.I., Agren, G.I., 2011. Modelling soil carbon development in Swedish coniferous forest soils-an uncertainty analysis of parameters and model estimates using the GLUE method. Ecol. Modell. 222 (17), 3020–3032.

Pan, M., et al., 2012. Multisource estimation of long-term terrestrial water budget for major global river basins. J. Climate 25 (9), 3191–3206.

Penman, H.L., 1948. Natural evaporation from open water, bare soil and grass, 193, pp. 120–145.

Pinault, J.L., Plagnes, V., Aquilina, L., Bakalowicz, M., 2001. Inverse modeling of the hydrological and the hydrochemical behavior of hydrosystems: characterization of karst system functioning. Water Resour. Res. 37 (8), 2191–2204.

Pohlheim, H. GEATbx.com Genetic and Evolutionary Algorithm Toolbox for Matlab GEATbx: Introduction Evolutionary Algorithms: Overview, Methods and Operators.

Potter, N.J., Zhang, L., Milly, P.C.D., McMahon, T.A., Jakeman, A.J., 2005. Effects of rainfall seasonality and soil moisture capacity on mean annual water balance for Australian catchments. Water Resour. Res. 41 (6).

Price, K., 2011. Effects of watershed topography, soils, land use, and climate on baseflow hydrology in humid regions: a review. Prog. Phys. Geography 35 (4), 465–492.

Querejeta, J.I., Estrada-Medina, H., Allen, M.F., Jimenez-Osornio, J.J., Ruenes, R., 2006. Utilization of bedrock water by Brosimum alicastrum trees growing on shallow soil atop limestone in a dry tropical climate. Plant Soil 287 (1–2), 187–197.

Sankarasubramanian, A., Vogel, R.M., 2002. Annual hydroclimatology of the United States. Water Resour. Res. 38 (6).

Scanlon, B.R., Mace, R.E., Barrett, M.E., Smith, B., 2003. Can we simulate regional groundwater flow in a karst system using equivalent porous media models? Case study, Barton Springs Edwards aquifer, USA. J. Hydrol. 276 (1–4), 137–158.

Schimel, D.S., Braswell, B.H., Parton, W.J., 1997. Equilibration of the terrestrial water, nitrogen, and carbon cycles. Proc. Natl. Acad. Sci. USA 94 (16), 8280–8283. https://doi.org/10.1073/pnas.94.16.8280.

Schwinning, S., 2008. The water relations of two evergreen tree species in a karst savanna. Oecologia 158 (3), 373–383.

Somma, F., Hopmans, J.W., Clausnitzer, V., 1998. Transient three-dimensional modeling of soil water and solute transport with simultaneous root growth, root water and nutrient uptake. Plant Soil 202 (2), 281–293.

Stedinger, J.R., Vogel, R.M., Lee, S.U., Batchelder, R., 2008. Appraisal of the generalized likelihood uncertainty estimation (GLUE) method. Water Resour. Res. 44.

Sun, M., et al., 2016. Uncertainty and sensitivity assessments of an agricultural-hydrological model (RZWQM2) using the GLUE method. J. Hydrol. 534, 19–30.

Tang, Y., Reed, P., Wagener, T., 2005. How effective and efficient are multiobjective evolutionary algorithms at hydrologic model calibration? Hydrol. Earth Syst. Sci. Discuss. 2 (6), 2465–2520.

Tetzlaff, D., et al., 2009. How does landscape structure influence catchment transit time across different geomorphic provinces? Hydrol. Processes 23 (6), 945–953.

Tritz, S., Guinot, V., Jourde, H., 2011. Modelling the behaviour of a karst system catchment using non-linear hysteretic conceptual model. J. Hydrol. 397 (3–4), 250–262.

Vrugt, J.A., Hopmans, J.W., Simunek, J., 2001. Calibration of a two-dimensional root water uptake model. Soil Sci. Soc. Am. J. 65 (4), 1027–1037.

Wang, Q.J., 1991. The genetic algorithm and its application to calibrating conceptual rainfall-runoff models. Water Resour. Res. 27 (9), 2467–2471.

Wang, S.J., Liu, Q.M., Zhang, D.F., 2004. Karst rocky desertification in southwestern China: geomorphology, landuse, impact and rehabilitation. Land Degrad. Dev. 15 (2), 115–121.

Wilcox, B.P., et al., 2008. Subsurface stormflow is important in semiarid karst shrublands. Geophys. Res. Lett. 35 (10). https://doi.org/10.1029/2008GL033696.

Williams, P.W., 2008. The role of the epikarst in karst and cave hydrogeology: a review. Int. J. Speleol. 37 (1), 1–10.

Xu, X., Liu, W., Scanlon, B.R., Zhang, L., Pan, M., 2013. Local and global factors controlling water-energy balances within the Budyko framework. Geophys. Res. Lett. 40, 6123–6129.

Yang, D., Sun, F., Liu, Z., Cong, Z., Lei, Z., 2006. Interpreting the complementary relationship in non-humid environments based on the Budyko and Penman hypotheses. Geophys. Res. Lett. 33 (18) n/a-n/a.

Yang, H.B., Yang, D.W., Lei, Z.D., Sun, F.B., 2008. New analytical derivation of the mean annual water-energy balance equation. Water Resour. Res. 44 (3). Artn W03410 doi: 10.1029/2007wr006135.

Yokoo, Y., Sivapalan, M., Oki, T., 2008. Investigating the roles of climate seasonality and landscape characteristics on mean annual and monthly water balances. J. Hydrol. 357 (3–4), 255–269.

Zeng, R.J., Cai, X.M., 2016. Climatic and terrestrial storage control on evapotranspiration temporal variability: analysis of river basins around the world. Geophys. Res. Lett. 43 (1), 185–195.

Zhang, L., Potter, N., Hickel, K., Zhang, Y.Q., Shao, Q.X., 2008. Water balance modeling over variable time scales based on the Budyko framework - model development and testing. J. Hydrol. 360 (1–4), 117–131.

Zhang, Y.Q., et al., 2016. Multi-decadal trends in global terrestrial evapotranspiration and its components. Sci. Rep. 6 Uk.

Zhang, Z., Chen, X., Ghadouani, A., Shi, P., 2011. Modelling hydrological processes influenced by soil, rock and vegetation in a small karst basin of southwest China. Hydrol. Processes 25 (15), 2456–2470.

Zhang, Z.C., Chen, X., Huang, Y.Y., Zhang, Y.F., 2014. Effect of catchment properties on runoff coefficient in a karst area of southwest China. Hydrol. Processes 28 (11), 3691–3702. https://doi.org/10.1002/Hyp.9920.